Stability Limit of Water by Metastable Vapor-Liquid Equilibrium with Nanoporous Silicon Membranes

*I-Tzu Chen[1], David A. Sessoms[1], Zachary Sherman[1], Eugene Choi[1], Olivier Vincent[1], Abraham D. Stroock[1,2]**

[1]Robert Frederick Smith School of Chemical and Biomolecular Engineering

[2]Kavli Institute at Cornell for Nanoscale Science

Cornell University, Ithaca, NY 14853

Abstract. Liquid can sustain mechanical tension as its pressure drops below the vapor-liquid coexistence line and becomes less than zero, until it reaches the stability limit – the pressure at which cavitation (i.e. the nucleation of vapor bubbles in bulk liquid) inevitably occurs. For liquid water, its stability limit is still a subject of debate: the results obtained by researchers using a variety of techniques show discrepancies between the values of stability limit and its temperature-dependence as temperature approaches 0°C. In this work, we present a study of the stability limit of water with the metastable vapor-liquid equilibrium (MVLE) method in which a volume of liquid is equilibrated with its unsaturated vapor via nanoporous silicon membrane. We also report on an experimental system which enables test of the temperature-dependence of the stability limit with MVLE. Our results falls in the range between -20 and -30 MPa; a range that is in consistent with the majority of the experiments but is far less negative than the limit obtained in experiments involving quartz inclusions and that predicted for homogeneous nucleation. Further, the stability limit we found increases monotonically (larger tension) as temperature approaches 0°C; this trend contradicts the centrifugal result of Briggs but agrees with the experiments by acoustic cavitation.

Introduction

When the pressure of a liquid is reduced below its saturation pressure, instead of forming vapor immediately, the liquid can exist in a metastable state[1]. In this situation, the liquid is superheated and, at pressures below zero, the liquid becomes stretched and is under mechanical tension. This generation of negative pressures in liquid water following isotherms is illustrated in Figure 1(A) and (B) (green lines with arrows). The metastable liquid will eventually "break" and return to stable equilibrium with vapor by cavitation, the nucleation of vapor bubbles, as the pressure falls to the cavitation limit – the pressure at which cavitation inevitably occurs. The behavior of liquid being under tension and its cavitation limit are relevant to various contexts in nature and technology, such as the transpiration and ascent of sap flow in trees[2], suckers on Cephalopod limbs[3], the drying stresses in unsaturated porous materials like soil and concrete[4–7], and hydrodynamic cavitation in hydraulic valves and around propeller blades[8,9]. Also, scientists have been pursuing the use of liquid at negative pressure in technologies: the mechanical suction pump invented in 1970 that was able to generate -0.07 MPa of pressure[10], the synthetic 'tree' that can continuous extract liquid water from sub-saturated vapor, transducing it into negative pressures liquid, and transporting it with large negative pressure gradient (21 MPa or higher)[11], and the MEMS-based loop heat pipes proposed to exploit negative pressure working fluid to achieve efficient heat transfer over long distance and against large acceleration[12].

Researchers have used a variety of techniques to placed liquid water under tension to measure the properties of liquid water at negative pressure and its cavitation limit (i.e., the stability limit)[13]. Numerous experiments have confirmed the existence of liquid water at the negative pressures, yet a picture of the structure of the phase diagram of water remains incomplete[14]. Understanding the phase diagram could help us explain the origin of the water's anomalies (e.g., a large increase of

isobaric heat capacity in the supercooled region). Different possible phase diagrams of water have been proposed (one can refer to a review by Debenedetti[14] for detailed descriptions and discussion for each scenarios). To discriminate between scenarios, many experiments with water or water proxies were conducted. Among these experiments, the recent work by Pallares *et al*.[15] with water-filled inclusions in quartz provided evidence for the hypothesis of a second critical point: at deep supercooling and positive pressures , and suggested that the negative pressure region is a promising experimental territory to put further constraints on or rule out remaining scenarios.

An extensive review on experimental methods studying water under tension can be found in recent reviews[13,16]. Here, we refer to a few widely-used methods: 1. Berthelot tube method[17,18], in which a rigid container (e.g. sealed glass capillaries and mineral crystal inclusions) filled with coexisting liquid and vapor in equilibrium is heated until the vapor bubble disappears, and then cooled following an isochoric path to decrease the liquid pressure until cavitation is observed. 2. Centrifugal method[19,20], based on the isothermal extension of water in z-shape tube rotating at high speed. Maximum tension is exerted at the axis of rotation due to the centrifugal force. 3. Acoustic method[16,21,22], a dynamic method to quench liquid water to negative pressure with standing or traveling acoustic waves. 4. Metastable vapor-liquid equilibrium (MVLE)[11,23,24], a method developed to mimic the transpiration mechanism by which the leaves generate the negative pressure that pulls sap up a tree; this method is illustrated in Fig. 1(C). As the internal bulk liquid water is placed in equilibrium with external sub-saturated vapor (vapor activity, a_{vap} = relative humidity/100 = $p_{vap}/p_{sat} < 1$, where p_{vap} [Pa] is the actual vapor pressure and p_{sat} [Pa] is the saturation vapor pressure on the binodal) through a porous membrane, its pressure, P_{liq} [Pa], will be below the binodal. The relationship between p_{vap} and P_{liq} can be estimated using Kelvin equation:

$$P_{liq} = p_{vap} + \frac{RT}{v_{liq}} \ln(a_{vap}) \quad (1)$$

where R [J mol^{-1}] is the ideal gas constant, T [K] is the temperature, and v_{liq} [m^3 mol^{-1}] is the molar volume of liquid water; see Theory section for more details.

The experimental measurements for water stability limits obtained with these different methods shows a large scatter, in particular at the temperature range from 50°C down to 0 °C. While the experiments in quartz inclusions[18,25] frequently measure stabilities as low as -140 MPa, consistent with that predicted by theory (e.g. the classical nucleation theory[1] predicts -168 MPa at room temperature for liquid volume of ~10 μm^3 and liquid lifetime of ~1 s) or simulations[26–28], the majority of the experiments have observed stability limits around -20 to -30 MPa[19,21,22,24,29–33], a far less negative value compared to theoretical predictions. Thus, in all the systems except for quartz inclusions, there is some other mechanism that limits stability and sets a "practical" stability limit. The mechanism for this limit has not been identified and represents an important outstanding question – fundamental and practical – about metastable liquid water. Further, among these experiments that show low stability, there are two sets of data showing contradictory temperature-dependence of the stability limit: Briggs[19] reported a remarkable 10-fold decrease in the maximum tension observed between 6°C and 0°C; in contrast to this abrupt change in the stability limit, Davitt *et al*.[32] found a monotonic increase (more negative) trend in the stability limit as temperature approached 0°C.

In this study, we report on an experimental system which enables test of the temperature-dependence of the stability limit with the MVLE method. In our previous work exploiting MVLE method[24], liquid water was encapsulated in vapor-coupled voids defined in hydrogel membranes. The sample reached metastable equilibrium with sub-saturated water vapor; activities of the vapor were established by the saturated salt solutions. The water remained stable with sub-saturated

vapor of activity, a_{vap} down to 0.85 at room temperature, corresponding to a stability limit of -22 MPa, based on Eq. 1, falling into the range typically reported by other techniques.

Here, we chose to change the materials and format of our samples to overcome challenges associated with using hydrogel as the membrane material; these challenges include the long equilibration time and difficulty controlling the volume and geometry of the internal volume of liquid. We turned to anodized silicon, an alternative nanoporous membrane material, as presented in our previous works of microtensiometer[34], cavition-coupled drying[4], and nano-confined flows[5]. We chose nanoporous silicon in this study for its preferred hydrophilic surface, its tunable porosity and pore structure, as well as its compatibility with standard micro-fabrication techniques. We fabricate free-standing porous silicon membranes and anodically bond them with glass substrates patterned with voids (Fig. 1(C)). These voids serve as vessels for water and are coupled to the water vapor through the porous silicon membrane. We also chose to control the activity of water with the pressure of pure water vapor in vacuum. This choice was made for two reasons: 1) exposing the samples to pure water vapor instead of air allowed us to minimize the dissolved gases in the bulk liquid water sample, and 2) controlling the water vapor pressure directly avoided complication of temperature-dependence of the activity of salt solutions – the suitable salts to achieve a desired series of activities becomes harder to find as the temperature approaches 0°C.

In this work, stability limit of water as a function of temperature from 15°C to 0°C is reported. We found the trend to be monotonically increasing as temperature approaches zero; this trend contradicts with the work by Briggs[19] but agrees with that observed in the study by Davitt *et al*.[32] Nevertheless, the observed stability limit is again less negative than the limit predicted for homogeneous nucleation from nucleation theories. A few possible mechanisms triggering

heterogeneous or seeded nucleation are discussed to try to explain the low stability limit observed in this work.

Theory

Metastable vapor-liquid equilibrium (MVLE). Fig. 1(C) illustrates the MVLE method in which a macroscopic volume of liquid confined in a closed container (void etched in glass) is coupled to the external vapor through a porous medium with rigid, wettable walls (porous silicon layer). When the vapor becomes sub-saturated (the activity of the vapor, $a_{vap} < 1$), the liquid evaporates from the membrane surface and liquid is pulled out of the void of a fixed volume; the cohesion of liquid water can resist this external mechanical tension (pulling) and results in a reduction of the internal liquid pressure. The pressure within the bulk liquid drops until the liquid in the void reaches metastable equilibrium with the sub-saturated vapor or cavitates. Capillarity ensure this equilibrium at the open ends of the pores. As the equilibrium is reached, the liquid pressure, P_{liq}, must satisfy the chemical potential balance, $\mu_{vap}(p_{vap},T) = \mu_{liq}(P_{liq},T)$:

$$\mu_{sat}(T) + \int_{p_{sat}}^{p_{vap}} v_{vap}(P,T)dP = \mu_{sat}(T) + \int_{p_{sat}}^{P_{liq}} v_{liq}(P,T)dP \quad (2)$$

where $\mu_{sat}(T)$ is chemical potential of water at the saturation pressure, p_{sat}, and temperature, T, and v_{vap} and v_{liq} are the molar volumes. Eq. 2 forms the basis for the approximate Kelvin equation (Eq. 1). If we assume that water vapor is an ideal gas, then Eq. 2 can be rewritten as:

$$RT\ln(a_{vap}) = \int_{p_{sat}}^{P_{liq}} \frac{1}{\rho_{liq}(P,T)} dP \quad (3)$$

where $\rho_{liq}(P,T)$ [mol m^{-3}] is the molar density of the liquid water that can be evaluated with an extrapolation of an equation of state (EoS). In this work, the translation between a_{vap} and P_{liq} under

MVLE is done through Eq. 3 with an extrapolation of the IAPWS EoS[35,36]. For a given temperature, we numerically integrated P_{liq}, starting from the saturation density ρ_{sat} to the spinodal density ρ_{min}, using trapezoid rule with a step size $\Delta\rho$=0.005. At each step, the (P_{liq}, a_{vap}) pair was recorded. The saturation vapor pressure data as a function of temperature, T from 235 to 400 K, was obtained from [Murphy & Koop, 2005][37] (235–273.15 K) and NIST[38] (273.16–400 K), and interpolated for any desired temperature within the range.

A pressure difference, $\Delta P = p_{vap} - P_{liq}$, arises as the two phases – sub-saturated vapor and metastable liquid – come to equilibrium. The ΔP can be calculated from the chemical potential balance described above. For example, for a 1% reduction in vapor activity from saturation (a_{vap} = 0.99) at room temperature, there exists a difference of pressure, $\Delta P \sim 1.3$ MPa. Such a co-existence of a liquid and its vapor at different pressures deviating from the binodal can be mediated with a porous medium with sufficiently small pore, based on capillarity. The Young-Laplace equation predicts that the pressure difference (the Laplace pressure) across a curved meniscus within a cylindrical pore,

$$p_{vap} - P_{liq} = \Delta P = \frac{2\sigma\cos\theta}{r_{pore}} \quad (4)$$

where σ [N m^{-1}] is the surface tension, θ [°] is the contact angle of liquid water with the pore wall, and r_{pore} [m] is the radius of the pore (see schematics for enlarged p ore surface in Fig. 1(C)). The porous medium with its associated menisci thus acts as a "membrane", in that it separates the bulk liquid and the bulk vapor phases while allowing equilibrium between them. The liquid water can pass through the membrane as a Darcy flow and transfer to and from the vapor phase via evaporation and condensation at the menisci; on the contrary, the vapor phase cannot penetrate the membrane as long as the menisci remain pinned within the pores based on the mechanical balance

in Eq. 4. The larger degree of sub-saturation in the vapor is (and the larger the reduction in pressure in the liquid is), the higher this Laplace pressure must be to sustain the pressure difference between the liquid and vapor phases, and the smaller the pore size must be. When the pressure difference required for equilibrium exceeds the Laplace pressure for the receding contact angle in any larger pores, these menisci will recede into the membrane and eventually allow vapor bubbles to enter the void ((a) in Fig. 2(A)-2(B) – meniscus invasion); the existence of a single path between the internal volume of liquid and the external vapor with pore size larger than a critical value ($r_{pore} > 2\sigma\cos\theta/\Delta P$) would result in the release of the metastability in the bulk liquid. For example, at ΔP = 20 MPa (corresponding to $a_{vap} \sim 0.86$ at room temperature), the largest pore size within the membrane is required to be no larger than $r_{pore} \sim$ 7nm.

Kinetic theory of the homogeneous nucleation. In the absence of a pre-existing pocket of gas in the liquid volume (e.g., in a structural defect – see below) or of invasion of gas through pore in the membrane, the metastable liquid may relax toward stable state via the formation (nucleation) of new vapor bubble within the bulk liquid (Fig. 2(B)-(e) – homogeneous nucleation). This nucleation event is an activated process that occurs when a thermal fluctuation overcomes the free energy barrier to form a bubble of the critical size (above which the bubble grows spontaneously).

Classical nucleation theory (CNT) lays the foundation of theoretical treatments of nucleation processes[1] – for droplet condensation from supercooled vapor, for crystallization in supercooled liquid, as well as for bubble nucleation in superheated liquid. Consider a liquid been put under tension at constant T to a pressure P_{liq}, the energy associated with creation of a vapor bubble of radius R [m] is given by[39]:

$$E(R) = \frac{4}{3}\pi R^3 (P_{liq} - p_{vap}) + 4\pi R^2 \sigma \quad (5)$$

where p_{vap} is the pressure of the vapor at the same chemical potential as the liquid at P_{liq}. The first term on the right hand side gives the energy gain through forming a volume of the stable phase, and the second term accounts for the energy cost of creating an interface with surface tension, σ [N m^{-1}]. The maximum of the energy profile in Eq. 5 gives an energy barrier,

$$E_b(P_{liq}) = \frac{16\pi\sigma^3}{3(P_{liq} - p_{vap})^2} \quad (6)$$

associated with the critical bubble of radius $r_c = 2\sigma / (p_{vap} - P_{liq})$. Thermal fluctuations of the system trigger the nucleation at a rate k_{cav} [s^{-1}], which can be expressed as

$$k_{cav} = \Gamma_0 V \exp(-\frac{E_b}{k_B T}) \quad (7)$$

where Γ_0 [m^{-3} s^{-1}] is a kinetic prefactor, V [m^3] is the volume of the bulk liquid, and k_B [J K^{-1}] is Boltzmann's constant. The probability that no cavitation event will occur during an experiment over time τ[16] is:

$$\Sigma = -\exp(-k_{cav} \cdot \tau) \quad (8)$$

The cavitation pressure P_{cav} at a given temperature T is defined as the liquid pressure at which the cavitation probability reaches 1/2,

$$P_{cav} = p_{vap} - \left(\frac{16\pi\sigma^3}{3k_B T \ln(\frac{\Gamma_0 V \tau}{\ln 2})} \right)^{1/2} \quad (9)$$

In this study, we compare the survival probability of voids in the sample against this theory to test the compatibility of our work with a thermally activated cavitation mechanism.

Other mechanisms of cavitation. One possibility for cavitation occurring before reaching the kinetic stability limit predicted by homogeneous nucleation theory is heterogeneous nucleation. Heterogeneous nucleation happens when the surface of the container in contact with the liquid (see

Fig. 2-(b) – hydrophobic patch) or an impurity within the liquid (see Fig. 2-(c) – impurity in water, such as suspended particles or dissolved solutes) provide a favorable nucleation site on which the formation of vapor starts. In many practical circumstances, cavitation events will be heterogeneous instead of homogeneous, due to the difficulty in avoiding any imperfectly wetted moieties or impurities within liquid. Heterogeneous nucleation can be described using the same formalism as described above for homogeneous nucleation, however it can have a lower energy barrier. For example, consider a hydrophobic surface in contact with the bulk liquid water as in Fig. 2-(b), the energy barrier to form a vapor bubble of critical size is given by[40]:

$$E_{het,b}(P_{liq}) = \frac{16\pi\sigma^3 F}{3(P_{liq} - p_{vap})^2} \quad (10)$$

where $F = (2 + 3\cos\theta - \cos^3\theta)/4$ and θ [°] is the equilibrium contact angle of water on the bulk solid surface. This expression differs from the one for the homogeneous nucleation only by the factor F, a function of contact angle, θ.

Another possibility for cavitation occurring before reaching the homogeneous stability limit is pre-nucleation due to the presence of gas bubbles trapped in the wall of the liquid container during the filling process (see Fig. 2-(d) – trapped bubble). As the liquid pressure drops, these bubbles can expand and result in a macroscopic vapor phase. Apfel's model[41] predicts the threshold pressure in the liquid, P_T, required to cause cavitation by the expansion of gas pockets trapped in idealized, conical crevices (as depicted in Fig. 2-(d)); this treatment is reasonable for the MVLE experiments exploiting a quasi-static application of tension. Depending on the crevice geometry (e.g. radius at the opening and apex angle), wettability of the liquid inside crevices (e.g. advancing and receding contact angle), and pressure history of the sample, different functional forms of the threshold pressure were predicted. For sufficiently large crevices, the gas content in the liquid and the application of elevated pressure during the preparation of the samples affect the threshold

pressure. There can also exist crevices of arbitrarily small size that lead to a threshold pressure that is independently of the pre-pressurization, and can be anywhere in the range between p_{vap} and $-2\sigma/r_0$. A detailed discussion exploring criteria of trapped bubbles effecting stability limit in MVLE can be found in [Wheeler & Stroock, 2009][24].

Experimental Methods

Sample fabrication. Fig. 1(C) shows the schematics of the porous silicon-glass void sample. The free-standing porous silicon membranes were anodically bonded to glass substrates patterned with voids; these voids served as vessels for water and are independently coupled to the water vapor through the porous silicon membrane.

Porous silicon was formed by anodization of silicon substrate in an HF-based electrolyte[42]. A partial dissolution of silicon occurs due to the electrochemical reaction at its surface. The porosified portion can be released from the substrate to form a free-standing layer with pores passing through its thickness[43]. Techniques of fabricating this free-standing silicon membrane have been described by many researchers[44–48]. These samples have mainly served for studying the optical and optoelectronic properties of porous silicon. A few different methods can be found in the literature, including a two-stage method[44,45] involving sharply raising the current density to the electropolishing region, a single-stage technique[46] in which porous layer is spontaneously detached, and a new two-step approach[48] consisting of gradually ramping the current density at a certain rate. We used the latter approach for its simplicity and its good control over the thickness and the porosity of the membrane.

Nanoporous silicon membranes were prepared by electrochemical anodic etching of highly doped, p-type, <100> oriented silicon wafers with a resistivity of 0.01 Ω-cm. Silicon wafers were

mounted, one at a time, between a Teflon cell and an Aluminum bottom electrode with one side of the silicon wafer in contact with the electrolyte, a 70:30 (v/v) solution of 49% hydrofluoric acid and 99% acetic acid in the Teflon cell. Fig. 3 shows the profiles of typical current density (Fig. 3(A)-left) and voltage (Fig. 3(A)-right) across the electrochemical etch cell, as well as schematic cross-section views of the silicon substrate during the etch process (Fig. 3(B)). With a Hewlett Packard DC power supply (Model 6634B), silicon substrate was etched at a constant current density of 13 mA cm^{-2} for 150 minutes, until the required thickness of porous layer was reached as assessed by total current passed per etched area; in our work, the etch rate = 1.18 [$\mu m\ (C/cm^2)^{-1}$]. Then, the current density was gradually ramped up at a constant rate of 90 mA $minute^{-1}$, to detach the porous layer from the substrate. As soon as the sign of membrane fully detaching was observed, etching was stopped. In Fig. 3(A)-right, the sudden drop of the voltage during the ramp reflects the full detachment of the porous layer into a free-standing membrane. The membrane taken out of the electrochemical cell was immersed in isopropanol for 5 minutes and then pentane for 5 minutes to reduce the stress during membrane drying. The final membrane thickness of the sample used in experiments reported here was measured by a Mitutoyo digital micrometer to be 138 μm.

BOROFLOAT® 33 float borosilicate glass wafers were used to define voids that we coupled to the porous silicon membrane. These voids were formed as follows: An amorphous silicon layer was deposited (Oxford PlasmaPro 100 PECVD) onto the glass wafer to a thickness of ~200 nm and then annealed to reduce the residual stress[49]. This layer served as the mask for the glass etch, and was patterned via standard lithography into a pattern of circular voids (200 μm in diameter) arranged in a square array of 25 × 25, with a distance of 400 μm between successive voids (Fig. 1(C) shows an array of 12 × 12 for the purpose of clarity). The voids were etched with 49%

hydrofluoric acid to reach a depth of 25 μm; the etch rate was 7 μm minute^{-1}. We then bonded the glass and silicon anodically (400°C, 800V) to couple each voids to the outside environment via the nanopores of the silicon membrane.

The bonded samples were submerged in water and left in the vacuum oven for 12 hours to remove air from the voids; this step was performed in order to avoid the large supersaturation with air in the liquid that would occur if one atmosphere of air were forced to dissolve in an equal volume of liquid. The samples were then filled with degassed water in a pressure bomb with 35 MPa of pressure to minimize residual gases in trapped bubbles.

Vapor control system. Fig. 4(A) shows the schematic diagram of the vapor control system. The custom sample stage was connected between the water vapor source and the vacuum pump, with needle valves on either side. As shown in the enlarged figure in Fig. 4(A), this aluminum stage consisted of a sample chamber on top of a cooling base. Two important features of the stage were: 1) the micro-grooves on the floor within the sample chamber in contact with the membrane-side of the sample; these grooves ensures good thermal contact between the silicon membrane and the sample chamber floor, and at the same time provide a macroscopic path way for the vapor to be equilibrium with the water in the membrane pore. 2) A recessed area in the ceiling of the cooling fluid cavity minimized the distance between the sample chamber floor and the cooling fluid; keeping a larger distance between the rest of the sample chamber and the cooling fluid also minimized condensation around the sample that could affect the vapor pressure. By adjusting the position of the two needle valves, one placed upstream and one placed downstream, we could control the vapor pressure within the sample chamber. The vapor pressure was measured with a capacitance pressure gauge (Adixen ASD2002). Water in the vapor source flask was degassed prior to the experiment to avoid abrupt boiling. The temperature of the vapor source immersion

bath (Lauda Brinkmann Ecoline100) was fixed at a value higher than that within the chamber to enable precise control of the vapor activity at values near saturation (relative humidity close to 100%) at the temperature of the sample. Cooling fluid to the stage was connected to an external temperature control bath (Thermo Scientific RTE 740) and circulated through the base of the stage to control the temperature at the sample. A resistance temperature detector (RTD) was inserted into a hole in the aluminum plate between the cooling fluid chamber and the sample chamber to measure the chamber floor temperature in real time. The sample was viewed using a stereoscope placed above the sample chamber's viewing window to observe the glass-side of the sample and the images were recorded over the duration of each experiment. To reduce condensation on the outer surface of the sample chamber, it was wrapped in insulating material and dry air was blown across the viewing window.

Fig. 4(B) and 4(C) show the temperature and pressure calibration data for the vapor control system. The temperature measurement was calibrated by observing the melting point, T_m, of pure liquids under atmospheric pressure on a piece of silicon wafer placed on the floor of the stage, as within our sample during experiments. Three different liquids were used – water (T_m = 0°C), cyclohexane (T_m = 6.47°C) and hexadecane (T_m = 17.05°C). As shown in Fig. 4(B), the measured melting points were compared with the known values of T_m to establish a temperature calibration line (the red dash line). The standard deviation of the temperature offsets from the calibration line was 0.14°C; this standard deviation was treated as uncertainty and was propagated to the uncertainty in vapor activity. The vapor pressure measurement was calibrated by observing the saturation pressure across the temperature range T = -1.5–18°C: the stage temperature was held at a constant value while the vapor pressure was gradually increased by adjusting the valves until liquid droplets emerged on the sample stage; we identified the pressure at the onset of condensation

as the saturation vapor pressure at the set temperature, $p_{sat}(T)$. Fig. 4(C) compares the measured pressures with the saturation pressures from the literature ([Murphy & Koop, 2005][37] and NIST[38]). We found no systematic offset of the measured pressures and hence we used no calibration line for pressure measurement; the standard deviation of pressure offsets was 4.4 Pa. For all the experiment data points ($T_{measured,}$ p_{vap}), we calibrate $T_{measured}$ using the temperature calibration line to obtain T_{actual}, and used p_{vap} as it is. The standard deviations of both temperature and pressure were treated as uncertainties and propagated to the uncertainty in vapor activity and liquid pressure (Figs. 7 and 9).

The experiment protocol for investigating stability limit was as follows: The temperature of the base of the chamber was set at a constant temperature prior to loading the sample. The bonded sample filled with liquid water was placed membrane-side down onto the floor of the chamber in the stage; a macroscopic film of liquid water was maintained near the sample to keep it hydrated during the assembly of the chamber. As the chamber was assembled and sealed, the vacuum pump was turned on to evacuate any air left in the chamber and start pulling pure water vapor into the system. The valves were adjusted to maintain the desired vapor pressure according to the activity set point. The duration for each activity was at least 3 hours before adjusting the valve to step down vapor pressure to a new set point; this duration was selected based on the observation that most cavitation events after a pressure step change happened within the first 90 minutes or less (see Fig. 6(A) and Results and Discussion – cavitation event history and survival probability curve). The cavitation events within glass voids and the subsequent emptying of liquid water were observed and recorded every 10 minute. We continued lowering the vapor pressure in step increments until all voids were cavitated and emptied.

Determination of probability of cavitation. Fig. 1(D) shows a snapshot of the sample top view during the course of the experiment. As shown, different states of the void are easily identifiable in these images: filled voids are almost entirely dark, emptied voids show a bright ring around the perimeter of the etched circle, and voids undergoing emptying have meniscus of the vapor bubble evolving in the center of the void. The time evolution of the number of the voids at each state (filled/emptying/emptied) was calculated with standard image analysis procedure using ImageJ and MATLAB. This cavitation history was then synchronized with the corresponding temperature and pressure data (an example of the cavitation history is shown in Fig. 6(A), see Results and Discussion – cavitation event history and survival probability curve). The synchronized data were used to produce the survival probability curve as a function of the water pressure (survival probability, Σ = number of filled voids/total number of voids), at each temperature.

Results and Discussion

Characterization of free-standing porous silicon membrane. The pore structure of the freestanding silicon membrane was observed with scanning electron microscopy (Fig. 5). The top view of the nanoporous silicon shows the opening of pores at the surface (dark spots) with diameters ranging from 3–8 nm; this range of pore size was confirmed by nitrogen adsorption porimetry (data not shown). The cross-sectional view shows the typical pore structure obtained in highly-doped, <100> oriented substrate – independent vertical pores with side branching. Assuming Darcy flow through the porous silicon membrane during the emptying of the voids, we estimated the hydraulic permeability, κ [m^2 (Pa· s)$^{-1}$], of the membrane based on Darcy's law,

$$Q = \frac{\Delta P}{R_{liq}} = \frac{-\kappa A(P_{liq} - p_{vap})}{L} \quad (11)$$

where Q [m^3 s^{-1}] is the volumetric flow rate, R_{liq} [Pa s m^{-3}] is the hydraulic resistance of the membrane saturated with liquid water, A [m^2] is the cross-sectional area to flow, and L [m] is the thickness of the porous membrane. The emptying time was not measured in detail in this work but has an upper bound of 10 minutes – the time frame between two consecutive images; once cavitated voids always emptied within one image frame. Due to this lack of temporal resolution, we can only estimate the hydraulic permeability of the membrane to be on the order of 10^{-18} m^2 $(Pa\cdot s)^{-1}$. In our previous work[4], the permeability for porous silicon was reported to be 1.44×10^{-17} m^2 $(Pa\cdot s)^{-1}$.

Cavitation event history and survival probability curve. After each step change in vapor pressure, new cavitation events started immediately and showed a decay in the number of events over time (Fig. 6(A)). We extracted a characteristic time for this decay by fitting to an exponential:

$$N(t) = N_0 \cdot \exp(-t / \tau_c) \quad (12)$$

where N is the number of cavitation events happened over a certain time frame (10 minutes) at time t, N_0 is the total number of cavitation events within the entire duration of one pressure step, and τ_c is characteristic time of decay. The average τ_c for all pressure steps was 92 minutes; therefore the time we allowed for equilibration in each pressure step (3 hours) was sufficient to ensure that the system was equilibrated and that the pressures within the voids were fully developed. This time scale of 92 minutes may be related to the pressure equilibration time, τ_{void}, of the bulk water in the voids to be in equilibrium with the external vapor,

$$\tau_{void} = R_{mem} \frac{V}{B} \quad (13)$$

where R_{mem} [Pa s m^{-3}] is the hydraulic resistance of the membrane and B [Pa] is the bulk modulus of liquid water. If we assumed the membrane to be entirely filled with liquid during the experiment, then $R_{mem} = R_{liq}$ and we could estimate τ_{void} based on the hydraulic permeability (as in the previous

section, Eq. 11). However, such estimation gives an equilibration time, τ_{void} on the order of seconds, in contrast to the tens of minutes observed for τ_c in Fig. 6(A). One hypothesis to explain this long equilibration time is that $R_{mem} = R_{liq} + R_{vap}$; while R_{liq} is the hydraulic resistance associated with the liquid water in pores, R_{vap} is the hydraulic resistance associated with the vapor in pores (see Fig. 6(B)) and can be estimated from Knudsen diffusion. The pores can be partially filled with vapor during the experiments; e.g., for pores of conical shape with the end of larger openings in contact with the external vapor, the menisci would gradually retreat deeper into the membrane to reach equilibrium at a smaller pore diameter as a_{vap} goes down (see Fig. 6(B). This possibility is supported by the SEM images observing the top and cross sectional view of the membrane (Fig. 5) – the membrane is asymmetrical: the pores are larger at the vapor side and are smallest at the top surface (bonded to the glass). Compare a single pore filled entirely with liquid or vapor, the ratio of R_{vap} / R_{liq} is estimated to be on the order of $10^{3.5}$. The time scale of τ_{void} considering the effect of vapor is on the order of tens of minutes, a value that is compatible with the scale of τ_c.

We note that a few cavitation events did continue to happen along the span of experiment. The small fluctuations in vapor activity (blue curve and the first vertical axis to the right) corresponds to non-negligible fluctuations in liquid pressure of ~1 MPa (red curve and the second vertical axis to the right) and may have provoked the continued cavitation at long times. Other cavitation mechanisms are also possible, and are discussed in the section – other mechanisms of cavitation.

At each temperature, we recorded the cavitation pressures of a total of 573 voids and plotted the survival probability, $\Sigma(P_{liq})$ – the probability that cavitation did not occur after the vapor activity was lowered to a given value. Fig. 7 shows the survival probability as a function of liquid pressure (calculated with Eq. 3) for four different temperatures. The 52 voids under bonding defects were excluded in the analysis (see Fig. 8(A), these defect voids are marked with cavitation threshold

$P_{liq} = 0$). We found that the lower the temperature, the higher the survival probability at a given P_{liq}. The lowest pressure in the liquid was observed at 0.3 °C and fell within the range of -25 to -30 MPa.

To analyze these survival curves further, we compared them to the predictions of CNT. According to CNT, the probability for survival (no cavitation), $\Sigma = \exp(-k_{cav} \cdot \tau)$ (Eq. 8), during an observation time τ in a cavity of volume V at pressure P_{liq}, where k_{cav} [s^{-1}] is the rate of nucleation:

$$\begin{aligned} k_{cav} &= \Gamma_0 V \exp\left(-\frac{E_b(P_{liq})}{k_B T}\right) \\ &= \Gamma_0 V \exp\left(-\frac{16\pi\sigma^3}{3(P_{liq} - p_{vap})^2 k_B T}\right) \end{aligned} \quad (14)$$

In Fig. 7(A), the dashed, black curve shows this prediction with the surface tension, σ, adjusted to match approximately the P_{cav} at 14.5°C. Clearly, the dependence on pressure predicted by CNT is dramatically more abrupt than observed in our system. This incompatibility with CNT differs from what was reported by Wheeler and Stroock[24] for analogous experiments in which a hydrogel served as the membrane: in those experiments, the shape of the transition was consistent with the prediction of the kinetic model of thermally activated nucleation. Such compatibility with CNT was also reported by for cavitation of liquid water with focused acoustic waves[32]. In work by our laboratory with a sample based on a porous silicon membrane with a distinct geometry from that used here, we did observe similarly broad transitions[4]. The samples in that study were distinct from those used here in having much thicker (72 fold) membrane between the voids and the external vapor. In that work, we successfully accounted for the breadth of the transition with a modified CNT model in which we allowed the effective surface tension to vary from void to void to account for spatial heterogeneities[4]. We hypothesized that the effective surface tensions vary across the population of voids within a narrow Gaussian distribution of mean value σ [N m^{-1}] and standard

deviation $\Delta\sigma$. With this hypothesis, we built a survival probability by convolving the prediction of CNT with this Gaussian distribution. The trend lines in Fig. 7(A) show, for each temperature, fits with this modified CNT with adjusted σ and $\Delta\sigma$. The surface tension σ and the ratio ($\Delta\sigma / \sigma$) we obtained at 4 different temperatures are summarized in Table. 1. These values of surface tension are of the same order of magnitude as those used to match the observed kinetics of cavitation of water by acoustic excitation[32]: they found an average (σ / σ_{bulk}) = 0.237 for temperatures ranging from 0 to 190°C, whereas the average value we find is 0.244. This value is also similar to that found by us previously for MVLE with porous silicon (0.256). The decrease of the distribution of surface tensions ($\Delta\sigma / \sigma$, Table 1) as temperature approaches zero is most likely due to the artifact that fewer data points were obtained during experiments at higher temperature.

We note, though, that the curves obtained with this model fail to capture the asymmetric shape of the data in our experiments – a smoother transition at lower tension and a steeper slope towards the more negative pressures. This observation suggests that the cavitation events in this work were not purely due to thermally activated nucleation, but rather to a mixture of the mechanisms. Hence, we choose to present in Fig. 7(B) the fits of the data with the standard logistic regression, to better represent the experimental data and to estimate more accurately the P_{cav} (the liquid pressure at which the survival probability $\Sigma = 0.5$) at each temperature:

$$\Sigma = 1 - \frac{1}{\left[1 + \left(\frac{e^{P_{liq}}}{e^{P_{cav}}}\right)^{b}\right]^{c}} \quad (15)$$

where b is the slope factor and c is the asymmetric factor. P_{cav}, b, and c were adjusted for each temperatures to obtain the trend lines. The values of P_{cav} for 4 different temperatures are reported in Table 1.

Spatial heterogeneity. The survival probability curves across different temperatures show similar shape, however, the breadth of the transition and its asymmetric shape suggest distinct mechanisms of cavitation may play a role in setting the observed threshold activity or liquid pressure for cavitation in different the voids across the sample. To explore this phenomenon, in Fig. 8(A) we present color maps showing the distribution of cavitation thresholds across the sample for experiments at different temperatures. We see in the pattern of threshold values that some voids repeatedly cavitated in the same range of tension; examples of a few such voids are marked with asterisks (*) in each frame in Fig. 8(A). The consistency in the threshold of these voids suggests that they contain persistent defects that render the cavitation deterministic. On the other hand the majority of the voids demonstrate apparently random changes in their thresholds from one run to another. To quantify this assessment, we analyze the correlation of cavitation thresholds for each voids between runs at different temperatures. The analysis consists in comparing the spatial maps of cavitation status for different runs at the same cavitated fraction, x (x = number of cavitated voids/total number of voids); the cavitation map records the status – either filled or cavitated (including emptying and emptied) – of each void at a given x. Two randomness indexes, α and β are used to compare the cavitation maps.

1) The α-index calculates the average correlation between two cavitation maps of the same cavitated fraction, x: if a void had the same status between two runs, it is assigned 1; if different, it is assigned 0. By averaging the assigned numbers over all voids we get the value of α (can be anywhere between 0 and 1), as a function of x. For comparison, the form of α-index for purely stochastic processes, $\alpha_{stoch} = x^2 + (1 - x)^2$; α_{stoch} is parabolic in x with a minimum of 0.5 at $x = 0.5$. Data points located above α_{stoch} indicate a positive correlation between the two cavitation matrixes;

below α_{stoch}, anti-correlation. The further away a point is from the $\alpha_{stoch}(x)$ at a given x, the more deterministic the process is.

2) The β-index is proposed to remove the dependency of randomness index on x, as in α-index; it is calculated using the equation $\beta = (\alpha(x) - \alpha_{stoch}(x)) / (1 - \alpha_{stoch}(x))$. For a process with a given degree of correlation, β is a constant value not dependent on x. The value of β is 0 for purely stochastic process and 1 for purely deterministic process. $\beta > 0$ indicates a positive correlation; $\beta < 0$, anti-correlation.

The α-index and β-index calculated for this work are compared to that for a purely stochastic process (solid red curves), and shown in Fig. 8(B) and (C); the data points shown summarize all comparisons between any two temperatures (a total of 6 pairs from 4 temperatures). As the cavitated fraction gets closer to 1, both the α and β indexes tend toward their values for a random process. This tendency is more apparent for β-index (Fig. 8(C)) as it flattens the dependence of α-index to x. These observations confirm the assertions above that, far from the cavitation threshold (lower tensions), the cavitation process occurs in a more deterministic manner whereas, as the experiment approaches the cavitation limit, the cavitation events become more random. We interpret the less random process as occurring due to structural defects in certain voids such as large pores that allow cavitation to occur by invasion of the meniscus (Fig. 2(B)-(a)). The more random behavior is compatible with a thermally-activated nucleation process. The shape of the survival probability curves also agrees with this interpretation: a steeper transition near the cavitation limit corresponds to thermally-activated process, and a less abrupt transition at lower tension correspond to cavitation induced by structural defects of varying concentrations or sizes.

Comparison of temperature-dependence of cavitation threshold across different methods. In Fig. 9, we report the largest tension (the most negative liquid pressure) observed at each

temperature in the experiments presented here along with the results obtained with other techniques[50]. The stability limit we obtained falls in the same range with all other experiments (except the quartz inclusion experiments of -140 MPa) and it varies monotonically as temperature approaches zero. This trend suggests again that the rapid loss of stability for temperatures below 10°C observed by Briggs[19] (red diamonds) was an artifact. The general trend of our work agrees with that of the work by Davitt *et al*.[32] (blue squares), with our thresholds occurring at ~3 MPa higher pressure (less negative) than found by the acoustic technique. This discrepancy is small compared to the discrepancy with respect to the quartz experiments, and may due to the different physics of the methods and some inherent systematic errors associated with different techniques used to evaluate the liquid pressure.

The large discrepancy between the results from MVLE experiments and from quartz experiments may due to a nearly ubiquitous cavitation mechanism(s) that imposes the highly reproducible values of stability limit between -20 to -30 MPa found with a variety of different techniques. Detailed discussions and analysis regarding the origin of this discrepancy can be found in several papers and reviews[13,24,25,51]. In brief, among the few mechanisms described in Fig. 2, mechanisms involving structural defects (e.g. hydrophobic patches – Fig. 2-(b), or bubbles trapped in the walls – Fig. 2-(d)) can be excluded, considering that 1) the absence of walls/boundaries in contact with the water sample in acoustic experiments, and 2) these mechanisms impose dependence of cavitation pressure on the distribution of defects and would result in a less abrupt transition in probability curve, in contradictory to the results obtained by Wheeler & Stroock[24]. Menisci invasion (Fig. 2-(a)) is not applicable to acoustic and shockwave experiments. One possible mechanism left to explain the discrepancy is the presence of dissolved or dispersed impurities in bulk water (Fig. 2-(c)). These floating impurities are unlikely to be dissolved gases,

in that 1) carefully degassed ultrapure water samples were used in the acoustic experiments and in this work, and 2) water samples saturated with various gases exhibit minor changes in the cavitation pressure[16]. In this work, the vacuum environment in which the experiments were performed further minimized the presence of dissolved gases in the samples. Nevertheless, there may be other destabilizing impurities present in the water used in all experiments that are eliminated in quartz inclusions during sample fabrication, or that are absorbed onto the walls of quartz and are deactivated. Potential candidates for this ubiquitous impurity have been proposed (e.g., hydronium ions); nevertheless, more experiments and simulations are required to further investigate this mechanism.

While some of the aforementioned mechanisms – Fig. 2-(a), (b) and (d) – are unlikely to be the mechanism(s) governing the low stability limits found with different techniques, we note that we cannot exclude the possibility that these mechanisms play some role in our experiments and affect the shape of the stability probability curves; discussion regarding the roles of these mechanisms in this specific work can be found in the next section (other mechanisms of cavitation).

Other mechanisms of cavitation. In this section we consider the mechanisms that could possibly explain the low stability limit and the shape of the survival possibility curves (Fig. 7) observed in this work, including menisci invasion (Fig. 2-(a)), heterogeneous nucleation (Fig. 2-(b) and (c)) and pre-nucleated bubbles (Fig. 2-(d)).

As described in Theory – metastable vapor-liquid equilibrium (MVLE), the largest, continuously connected pore coupling a void to the outside vapor would determine the maximum tension sustainable in the liquid within the void. Once the water meniscus in the pore walls reaches its receding contact angle, the pore water begins to retract and eventually the void starts to dry out once the meniscus reaches the inner end of the pore. Although the pore size and the pore structure

of nanoporous silicon membranes are fairly uniform (as shown in the SEM images, Fig. 5, and porimetry results), a few larger pores may exist across the membrane surface and govern the stability limit of the voids coupled to them. For example, water within a pore with a smallest effective pore diameter r_{pore} = 10 nm would recede into the void at $P_{liq} \sim$ -13.3 MPa for a receding contact angle, $\theta = 25°$.[5] Structural defects inherent in the porous silicon membrane most likely contribute to the few voids that repeatedly cavitated at lower tensions, and hence resulted in the gentle decrease observed in survival probability curves at pressures far above (less negative) than the stability limit.

To consider the possibility of that heterogeneous nucleation occurs on hydrophobic patches, it is essential to gain knowledge regarding the hydrophobicity of the materials used to fabricate the sample. Both the borosilicate glass and the porous silicon are considered to be hydrophilic; however, only the macroscopic contact angle of water on the bulk surface of these materials were reported to be from 0–40°.[5,52,53] The contact angle of water at the pore walls within the porous silicon is difficult to characterize; while the wetting behavior of water and other liquids is consistent with the bulk contact angle, we cannot exclude the possibility that there exist highly hydrophobic patches on the membrane side walls – e.g., hydrogen bond terminated Si surface instead of oxide – that are small enough and at sufficiently low density to have had a weak impact on the macroscopic contact angle or wetting behavior. Heterogeneous nucleation can also occur on impurities floating in the bulk liquid; we cannot exclude the possibility that some impurities inevitably dissolved into the water and effect the shape of the stability curves.

The possibility of pre-nucleated vapor bubbles trapped in large crevices and affect the stability limit is unlikely. Our previous experiments suggested that the cavitation threshold would be equal or larger in magnitude than the pre-pressure; the pre-pressurization of samples in this work was

done at 35 MPa. The magnitude of this pre-pressure is larger than that of the cavitation threshold for the most stable void observed (~-30 MPa). Any bubbles trapped in large crevice within the samples should either be completely dissolved into the water or reside in the crevices and would not attain the critical size to cause cavitation at the tensions observed. However, as discussed in the Theory section, there may be "calibrated" crevices of arbitrarily small sizes that could lead to a threshold pressure only depending on the geometry of the crevices and the wetting properties, and be independent of the pre-pressure[24].

All the aforementioned defects or impurities may have a non-uniform size or concentration distribution across the voids and may enter the voids in a random manner during each refilling, and hence result in a relatively broad probability curve. To confirm or exclude any of these mechanisms, further experiments are needed. We note however that the cavitation pressures observed on most stable voids at different temperatures are most likely due to the dominate mechanism that is the same in various experiments, and the general trend of the stability limit as a function of temperature presented in this work is probably not affected by these other mechanisms for nucleation.

Conclusions

We used the metastable vapor-liquid equilibrium method with a nanoporous silicon membrane to investigate the stability limit of liquid water as a function of temperature from 15°C to 0°C. We found the stability limit to be monotonically increasing (more negative) as temperature approached 0°C; this trend contradicts the famous results of Briggs but agrees with the experiments by acoustic cavitation. Nonetheless, our results lie within the range of -20 MPa to -30 MPa; this limit is far less negative than the limit predicted for homogeneous nucleation.

The vapor control system introduced in this work opens up the possibility of studying stability limit of water at temperatures further down below zero, into the doubly metastable region on water's phase diagram (supercooled and negative pressure). Experiments investigating water properties in this region can potentially shed light on water's anomalies[15]. Also, the porous silicon membrane provides a practical platform to reliably place a static, bulk volume of liquid into metastable region that can be studied, manipulated and coupled to existing technologies – e.g., MEMS-based loop heat pipes[12] for the transfer of heat with liquids at negative pressures, and tensiometers[34] for measuring water potentials in plants and soils.

Acknowledgement. We thank Glenn Swan for technical assistance. This work was supported by the Air Force Office of Scientific Research (FA9550-15-1-0052) and the Camille Dreyfus Teacher-Scholar Awards program and was performed in part at the Cornell NanoScale Facility, a member of the National Nanotechnology Coordinated Infrastructure (NNCI), which is supported by the National Science Foundation (Grant ECCS-15420819). Z.S. acknowledges partial support from the Cornell College of Engineering's Education Learning Initiatives.

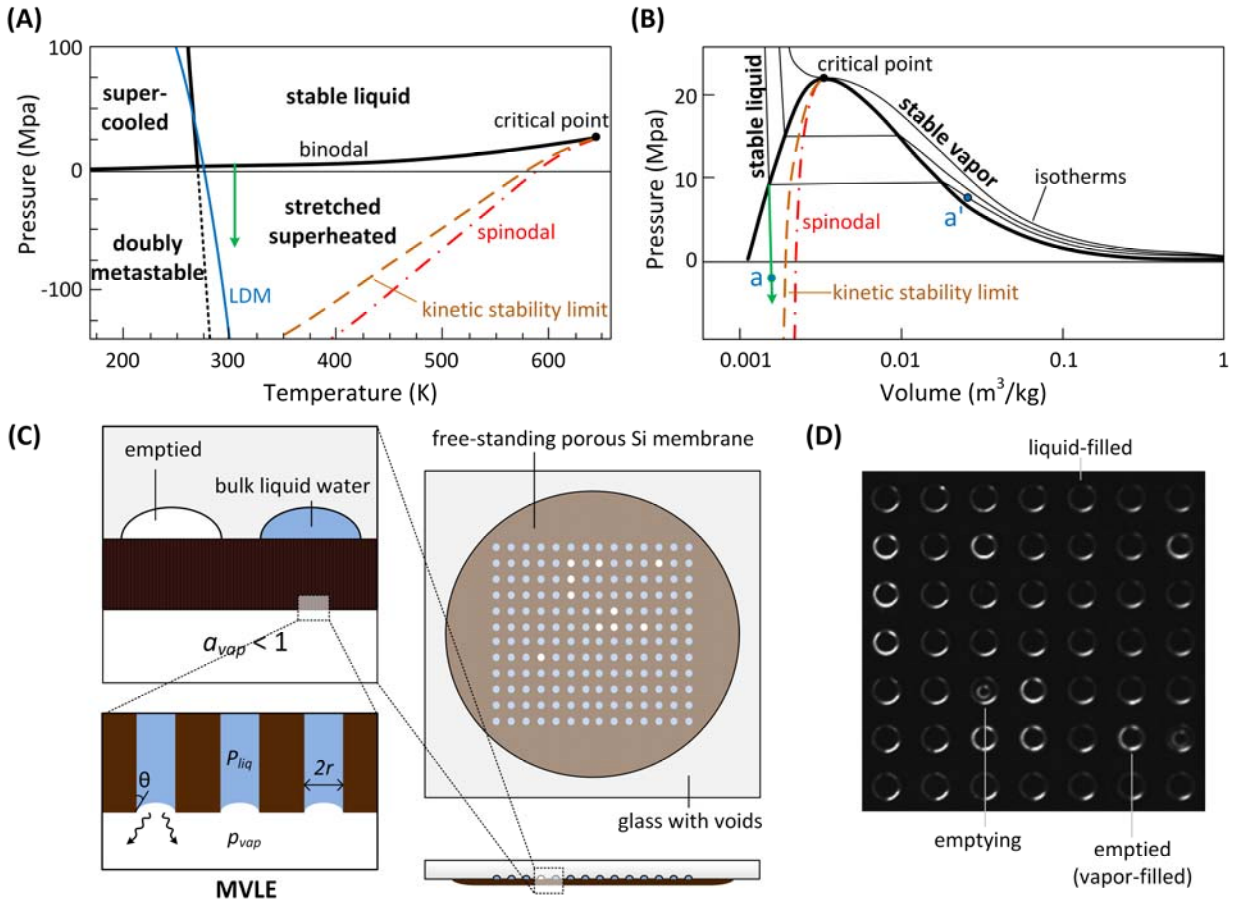

Figure 1. Phase diagram of water and metastable vapor-liquid equilibrium (MVLE). (A) Schematic Pressure-Temperature cut showing the binodal (thick black solid curve), the spinodal (red dashed-dot curve), and an isotherm (green line with arrow) illustrating the generation of the metastable state of superheated liquid water under tension. The spinodal is the thermodynamic stability limit of a metastable liquid. Beyond the spinodal the liquid is no longer mechanically stable. The blue solid curve is the line of liquid density maxima (LDM). The kinetic stability limit predicted by homogeneous nucleation theory is represented as the dashed curve positioned between the binodal and spinodal. (B) Schematic Pressure-Volume cut showing the vapor-liquid coexistence dome (thick black solid curve) and isotherms (thin black solid curves). The green curve with an arrow illustrates the generation of metastable liquid water; the pairs of blue points

indicate liquid states (a) in metastable equilibrium with sub-saturated vapor (a'). (C) Schematic diagrams showing the top and cross-sectional views of a nanoporous silicon membrane bonded with glass to define the voids in the sample. The enlarged figures illustrate the MVLE method: a nanoporous silicon membrane saturated with liquid water separates the bulk liquid water within glass voids from the external sub-saturated vapor with activity, $a_{vap} < 1$. At the membrane surface, the liquid water in pores and the sub-saturated vapor satisfy the chemical potential balance, $\mu_{liq}(P_{liq},T) = \mu_{vap}(p_{vap},T)$. The pressure of the water under the concave meniscus is $P_{liq} = p_{vap} - 2\sigma\cos\theta/r$, where σ [N m^{-1}] is the surface tension, θ [°] is the contact angle of liquid water with the pore wall, and r [m] is the radius of the pore. (D) An actual device image (top view) shows liquid-filled, emptying, and vapor-filled cavities.

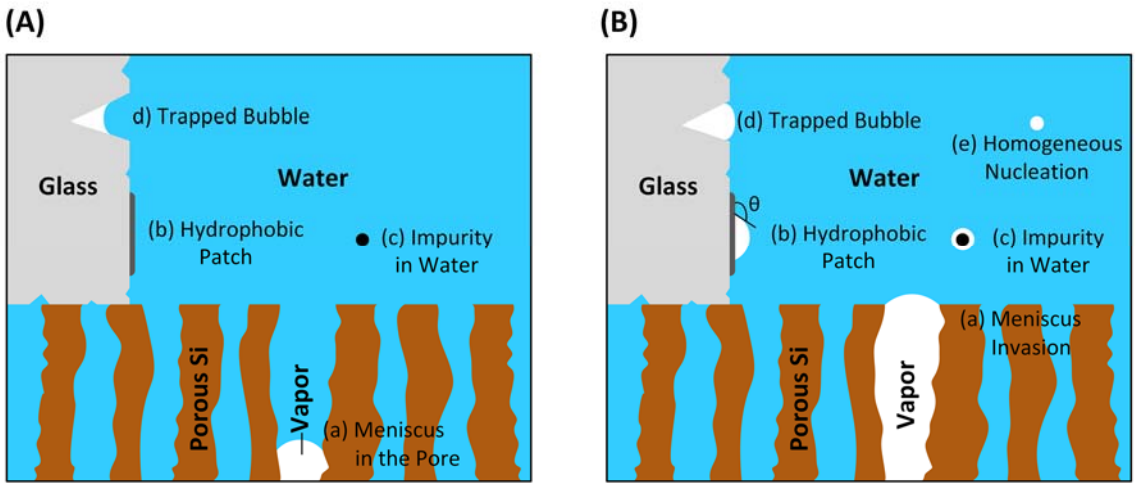

Figure 2. Mechanisms of cavitation. (A) Illustration of features in a glass void bonded to porous silicon membrane that potentially lead to cavitation thresholds above the kinetic stability limit imposed by homogeneous nucleation, including (a) invasion of meniscus in a large pore, (b) heterogeneous nucleation on a hydrophobic patch on the surface of the void, (c) heterogeneous nucleation on a dissolved or dispersed impurity, and (d) pre-nucleation by a bubble trapped in a crevice on the void wall. (B) As the bulk water in the void is placed at sufficiently reduced pressures, cavitation may occur due to (a) meniscus receding into the void, or features (b)-(d), or (e) homogeneous nucleation.

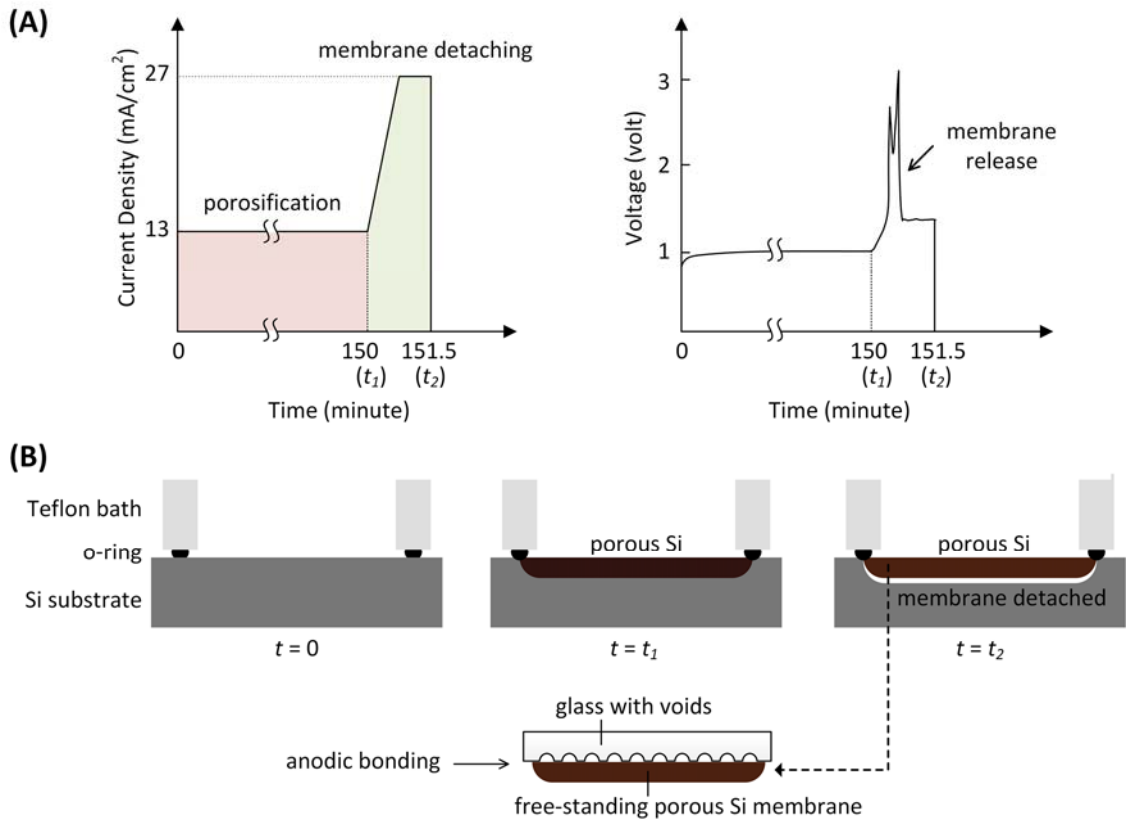

Figure 3. Fabrication of free-standing porous silicon membrane and membrane-coupled voids. (A) The temporal profile of imposed current density (left) and an example of a typical measured voltage profile (right) during the phases of the porosification and the ramping of current density to detach the porous layer. (B) Cross-sectional view of silicon wafer under electrochemical etch cell at corresponding time points and the subsequent bonding with etched glass.

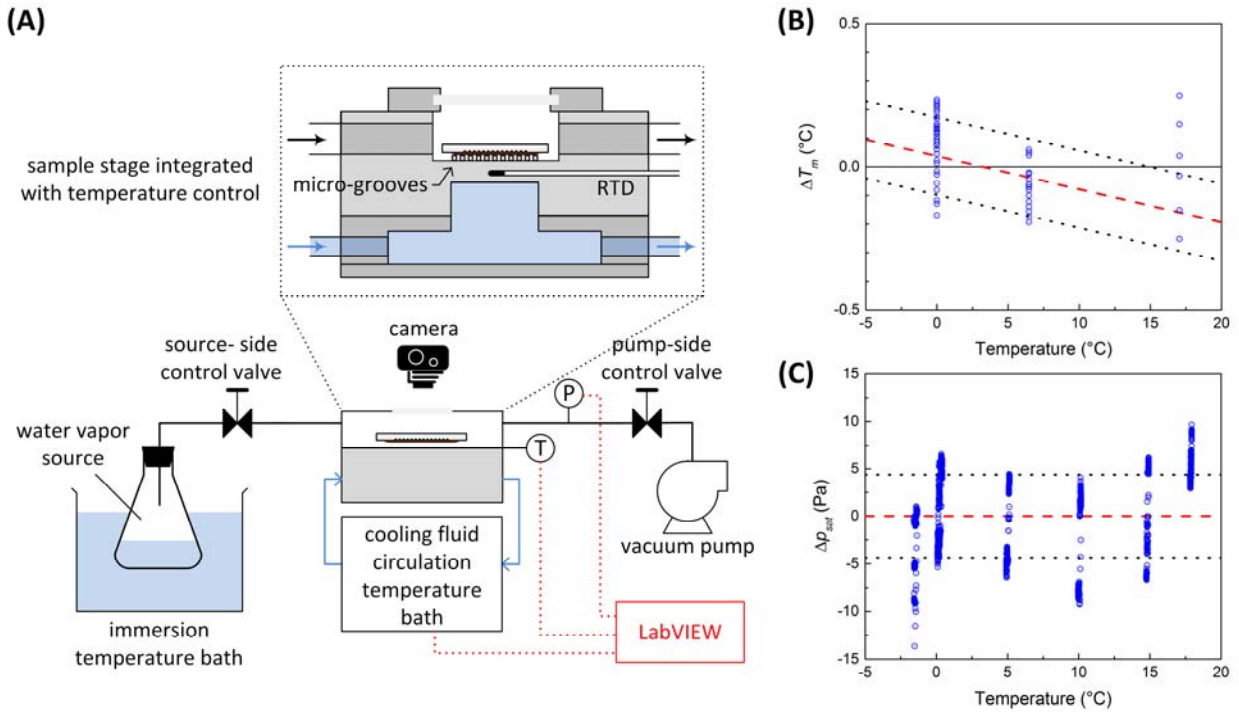

Figure 4. Vapor control system. (A) Schematic diagrams of the experimental system. The temperature and pressure within the chamber were automated to record every 2 seconds using LabVIEW. The expanded view (top) shows the detail of a custom-built sample stage. (B) Temperature calibration data. Blue circles represent the differences in measured melting temperatures relative to literature values, ΔT_m = (measured melting points – T_m), for three liquids – water (T_m = 0°C), cyclohexane (T_m = 6.47°C), and hexadecane (T_m = 17.05°C). The red dash line presents the calibration line obtained from the data and the black dot line shows the standard deviation of the data from the calibration line. This calibration line was used to calibrate all temperature measurements in this work; $T_{actual} = 0.992 \times T_{measured} + 0.0567$. (C) Pressure calibration data. Blue circles represent the differences in measured saturation pressures from literature values, Δp_{sat} = (measured saturation pressure(T) – $p_{sat}(T)$); the temperature corresponding to each data point is calibrated using the temperature calibration line.

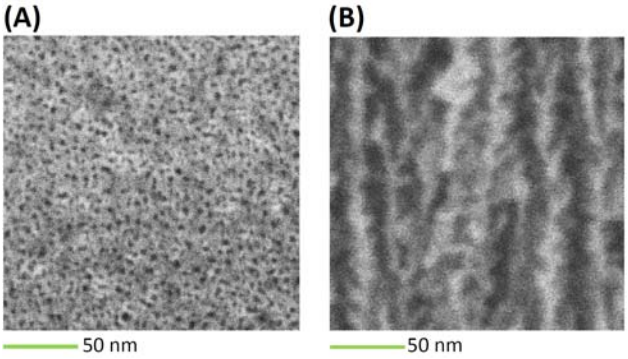

Figure 5. Top (A) and cross-sectional (B) views of the free-standing porous silicon membrane taken by scanning electron microscopy (SEM). The pore size observed from the top view is at the 5 nm-diameter range; this side of the porous silicon membrane is bonded to the glass. From the cross-sectional view, the channels have variable pore diameters ranging from ~5–20 nm.

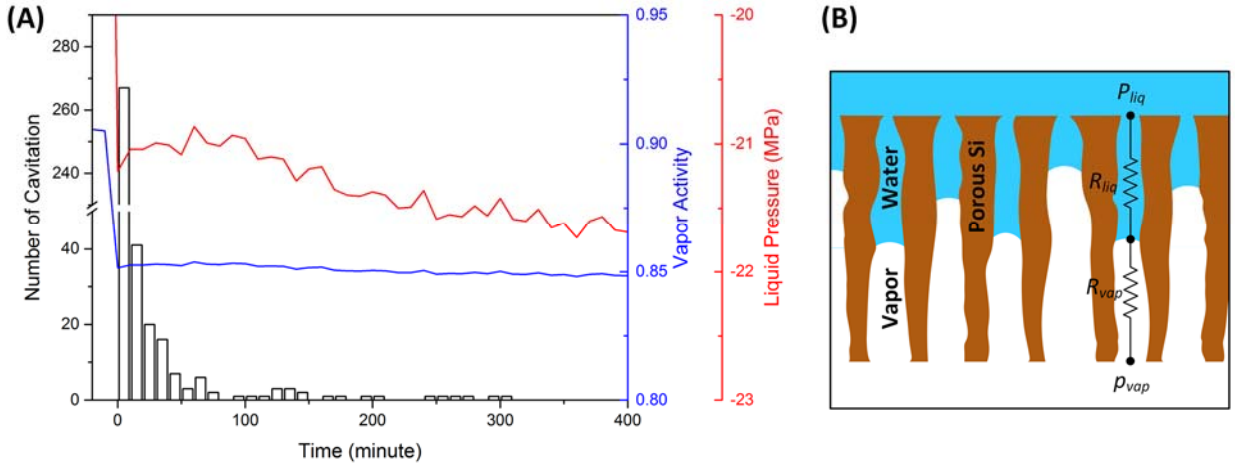

Figure 6. Temporal evolution of cavitation events. (A) Part of the cavitation history at T = 14.5°C showing the evolution of cavitation events (counted every 10 minutes) after a step change in the vapor pressure from a_{vap} = ~0.9 to ~0.85. The blue axis (right) is the vapor activity calculated from the vapor pressure data acquired in real time. The red axis (right) is the corresponding liquid pressure P_{liq} (Eq. 3). (B) Schematic diagram illustrating menisci receding from the porous silicon membrane edge in a membrane with irregular shape pores. The liquid water and vapor phases within the pores contribute to the overall hydraulic resistance, R_{total}, with R_{liq} and R_{vap}, respectively. The aspect ratio of the pores is exaggerated in this diagram.

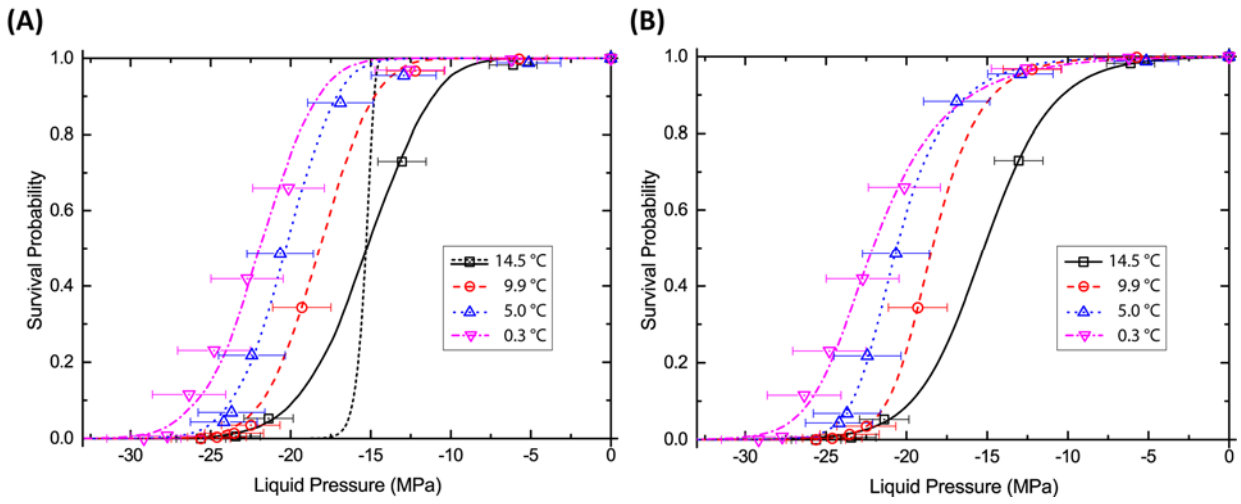

Figure 7. Survival probability (Σ) for water in porous silicon/glass sample as a function of the liquid pressure (P_{liq}). The pressure was translated from vapor activity (a_{vap}) using IAPWS EoS (Eq. 3). (A) The dashed, black curve shows the prediction of CNT (Eq. 8) with σ as the only adjustable parameter. The other trend lines for all four temperatures are fits with the modified CNT with adjusted σ and $\Delta\sigma$. (B) Survival probability with trend lines that are least-squares fits to the survival probability data at each temperatures using the standard logistic regression (Eq. 15).

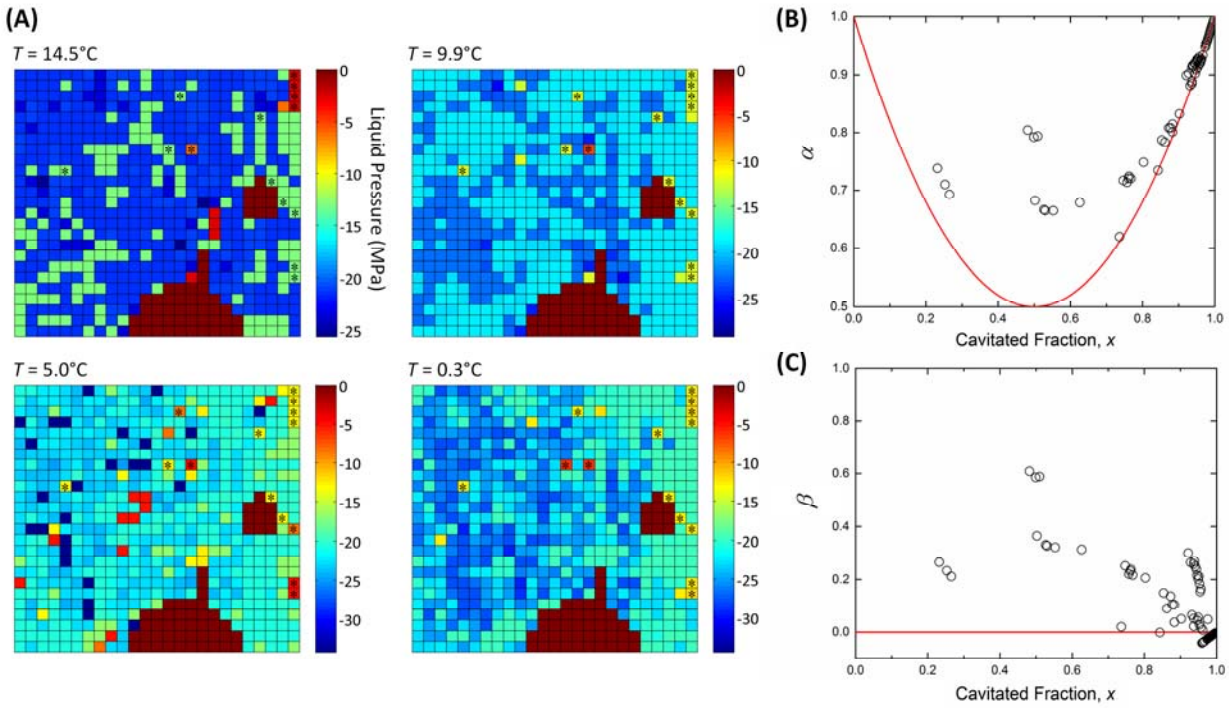

Figure 8. Variations in cavitation threshold. (A) Spatial color maps showing cavitation threshold for each voids at T = 14.5°C, 9.9°C, 5.0°C, and 0.3°C. Two areas of voids (near middle right and near bottom center) were defective due to bonding, and were excluded during data analysis. The color of each voids corresponds to the value of P_{liq} at which cavitaion initiated. The color bars represent the liquid pressure, P_{liq} over the range from p_{sat} (a_{vap} = 1) to 2 × P_{cav}. The voids marked with asterisks (*) were voids that repeatedly cavitated at the same range of relatively low tensions in each run. (B-C) Correlation indices (α-index in (B) and β-index in (C) – see text) for thresholds across the four runs as a function of the cavitated fraction, x.

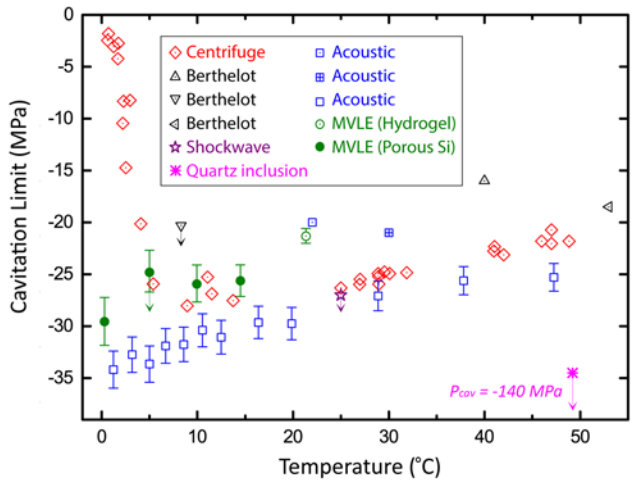

Figure 9. Comparison of the largest tension (the most negative pressure) of liquid water as a function of temperature obtained with different techniques (adapted from [Caupin *et al.*, 2012][50], added data points from this work for comparison): z-tube centrifuge (red diamonds); Berthelot-Bourdon tubes (triangle up and triangle down); metal Berthelot tube with pressure transducer (triangle facing left); shock wave (purple star); acoustic (blue squares); and MVLE in synthetic trees (green circle) and in free-standing porous Si sample (green solid circles). A short arrow on data points means that the cavitation limit in that specific experiment was not yet reached. Result from one Quartz inclusion experiment (pink asterisk) is indicated on the graph with a long arrow pointing the observed cavitation limit of -140 MPa. On the data points for porous silicon (green solid circles), the uncertainty of temperature calibration were smaller than the symbol width; the vertical error bars represent the uncertainty based on the propagation of the standard deviation of both the temperature and the pressure calibration.

T [°C]	14.5	9.9	5.0	0.3
σ [N m^{-1}]	0.0161	0.0178	0.0191	0.0200
$\Delta\sigma/\sigma$	15%	10%	9%	9%
σ / σ_{bulk}	0.217	0.240	0.255	0.264
P_{cav} [MPa]	-15.3	-18.5	-20.7	-22.1

Table 1. Fitting parameters for different temperatures

*Corresponding author. E-mail: ads10@cornell.edu.

References

(1) Debenedetti, P. G. Metastable Liquids: Concepts and Principles. **1996**, 411.

(2) Nobel, P. S. *Physicochemical and Environmental Plant Physiology*, Third Edit.; Academic Press, 2005.

(3) Smith, A. M. Negative Pressure Generated By Octopus Suckers: A Study of the Tensile Strength of Water in Nature. *J. Exp. Biol.* **1991**, *157* (1), 257–271.

(4) Vincent, O.; Sessoms, D. A.; Huber, E. J.; Guioth, J.; Stroock, A. D. Drying by Cavitation and Poroelastic Relaxations in Porous Media with Macroscopic Pores Connected by Nanoscale Throats. *Phys. Rev. Lett.* **2014**, *113* (3), 1–5.

(5) Vincent, O.; Szenicer, A.; Stroock, A. D. Capillarity-Driven Flows at the Continuum Limit. *Prepr. arXiv1510.00411* **2015**, 1–5.

(6) Stroock, A. D.; Pagay, V. V; Zwieniecki, M. A.; Michele Holbrook, N. The Physicochemical Hydrodynamics of Vascular Plants. *Annu. Rev. Fluid Mech.* **2014**, *46* (1), 615–642.

(7) Brinker, C. J.; Scherer, G. W. *Sol- Gel Science: The Physics and Chemistry of Sol-Gel Processing*; Academic press, 1990.

(8) Arndt, R. E. . Cavitation in Fluid Machinery and Hydraulic Structures. *Annu. Rev. Fluid Mech.* **1981**, *13* (1), 273–326.

(9) Franc, J.-P.; Michel, J.-M. *Fundamentals of Cavitation*; Springer Science & Business Media, 2006.

(10) Hayward, A. Mechanical Pump with a Suction Lift of 17 Metres. *Nature* **1970**.

(11) Wheeler, T. D.; Stroock, A. D. The Transpiration of Water at Negative Pressures in a

Synthetic Tree. *Nature* **2008**, *455* (7210), 208–212.

(12) Chen, I. T.; Pharkya, A.; Stroock, A. D. Analysis of Superheated Loop Heat Pipes Exploiting Nanoporous Wick Membranes. *AIChE J.* **2014**, *60* (2), 762–777.

(13) Caupin, F.; Stroock, A. The Stability Limit and Other Open Questions on Water at Negative Pressure. *Liq. Polymorph. Adv. Chem. Phys.* **2013**, *152*, 51–80.

(14) Debenedetti, P. G. Supercooled and Glassy Water. *J. Phys. Condens. Matter* **2003**, *15* (45), 1669–1726.

(15) Pallares, G.; El Mekki Azouzi, M.; Gonzalez, M. A.; Aragones, J. L.; Abascal, J. L. F.; Valeriani, C.; Caupin, F. Anomalies in Bulk Supercooled Water at Negative Pressure. *Proc. Natl. Acad. Sci.* **2014**, *111* (22), 7936–7941.

(16) Herbert, E.; Balibar, S.; Caupin, F. Cavitation Pressure in Water. *Phys. Rev. E - Stat. Nonlinear, Soft Matter Phys.* **2006**, *74* (4), 1–22.

(17) Berthelot, M. Sur Quelques Phénomènes de Dilatation Forcée Des Liquides. *Ann. Chim. Phys.* **1850**, *30*, 232–237.

(18) Zheng, Q.; Durben, D. J.; Wolf, G. H.; Angell, C. A. Liquids at Large Negative Pressures: Water at the Homogeneous Nucleation Limit. *Science* **1991**, *254* (5033), 829–832.

(19) Briggs, L. J. Limiting Negative Pressure of Water. *J. Appl. Phys.* **1950**, *21* (7), 721–722.

(20) Cochard, H.; Barigah, T.; Herbert, E.; Caupin, F. Cavitation in Plants at Low Temperature: Is Sap Transport Limited by the Tensile Strength of Water as Expected from Briggs' Z-Tube Experiment? *New Phytol.* **2007**, *173* (3), 571–575.

(21) Galloway, W. J. An Experimental Study of Acoustically Induced Caviation in Liquids. *J. Acoust. Soc. Am.* **1954**, *26* (5), 849–857.

(22) Greenspan, M.; Tschiegg, C. E. Radiation-Induced Acoustic Cavitation; Apparatus and

Some Results. *J. Res. Natl. Bur. Stand., Sect. C* **1967**, *71*, 299.

(23) Machin, W. D.; Stuckless, J. T. Capillary-Condensed Water in Silica Gel. *J. Chem. Soc. Faraday Trans. 1* **1985**, *81* (3), 597.

(24) Wheeler, T. D.; Stroock, A. D. Stability Limit of Liquid Water in Metastable Equilibrium with Subsaturated Vapors. *Langmuir* **2009**, *25* (13), 7609–7622.

(25) Azouzi, M. E. M.; Ramboz, C.; Lenain, J.-F.; Caupin, F. A Coherent Picture of Water at Extreme Negative Pressure. *Nat. Phys.* **2013**, *9* (1), 38–41.

(26) Haar, L.; Gallagher, J. S.; Kell., G. S. *National Bureau of Standards-National Research Council Steam Tables*; CRC Press, 1984.

(27) Poole, P. H.; Sciortino, F.; Essmann, U.; Stanley, H. E. Phase Behaviour of Metastable Water. *Nature* **1992**, *360* (6402), 324–328.

(28) Yamada, M.; Mossa, S.; Stanley, H. E.; Sciortino, F. Interplay between Time-Temperature Transformation and the Liquid-Liquid Phase Transition in Water. *Phys. Rev. Lett.* **2002**, *88* (19), 195701.

(29) Henderson, S. J.; Speedy, R. J. A Berthelot-Bourdon Tube Method for Studying Water under Tension. *J. Phys. E.* **1980**, *13* (7), 778–782.

(30) Henderson, S.; Speedy, R. Temperature of Maximum Density in Water at Negative Pressure. *J. Phys. Chem.* **1987**, *17* (6), 3062–3068.

(31) Hiro, K.; Ohde, Y.; Tanzawa, Y. Stagnations of Increasing Trends in Negative Pressure with Repeated Cavitation in Water/Metal Berthelot Tubes as a Result of Mechanical Sealing. *J. Phys. D. Appl. Phys.* **2003**, *36*, 592–597.

(32) Davitt, K.; Arvengas, A.; Caupin, F. Water at the Cavitation Limit: Density of the Metastable Liquid and Size of the Critical Bubble. *EPL (Europhysics Lett.* **2010**, *90*, 16002.

(33) Larter, M.; Brodribb, Timothy, J.; Pfautsch, S.; Burlett, R.; Cochard, H.; Delzon, S. Extreme Aridity Pushes Trees to Their Physical Limits. *Plant Physiol.* **2015**, *168* (July), pp.00223.2015.

(34) Pagay, V.; Santiago, M.; Sessoms, D. A.; Huber, E. J.; Vincent, O.; Pharkya, A.; Corso, T. N.; Lakso, A. N.; Stroock, A. D. A Microtensiometer Capable of Measuring Water Potentials below -10 MPa. *Lab Chip* **2014**, *14* (15), 2806–2817.

(35) Wagner, W.; Pruß, A. The IAPWS Formulation 1995 for the Thermodynamic Properties of Ordinary Water Substance for General and Scientific Use. *J. Phys. Chem. Ref. Data* **1999**, *31* (2), 387.

(36) The International Association for the Properties of Water and Steam. Revised Release on the IAPWS Formulation 1995 for the Thermodynamic Properties of Ordinary Water Substance for General and Scientific Use, September 2009.

(37) Murphy, D. M.; Koop, T. Review of the Vapour Pressures of Ice and Supercooled Water for Atmospheric Applications. *Q. J. R. Meteorol. Soc.* **2005**, *131* (608), 1539–1565.

(38) Lemmon, E. W.; McLinden, M. O.; Friend, D. G. Thermophysical Properties of Fluid Systems. In *NIST Chemistry WebBook, NIST Standard Reference Database Number 69, Eds. P.J. Linstrom and W.G. Mallard*; National Institute of Standards and Technology: Gaithersburg MD, 20899.

(39) Fisher, J. C. The Fracture of Liquids. *J. Appl. Phys.* **1948**, *19* (11), 1062–1067.

(40) Blander, M.; Katz, J. L. Bubble Nucleation in Liquids. *AIChE J.* **1975**, *21* (5), 833–848.

(41) Apfel, R. E. The Role of Impurities in Cavitation-Threshold Determination. *J. Acoust. Soc. Am.* **1970**, *48* (5B), 1179.

(42) Canham, L. *Handbook of Porous Silicon*; Springer, 2014.

(43) Turner, D. R. Electropolishing Silicon in Hydrofluoric Acid Solutions. *J. Electrochem. Soc.* **1958**, *105* (7), 402–408.

(44) Mauckner, G.; Rebitzer, W.; Thonke, K.; Sauer, R. Quantum Confinement Effects in Absorption and Emission of Freestanding Porous Silicon. *Solid State Commun.* **1994**, *91* (9), 717–720.

(45) Ghulinyan, M.; Oton, C. J.; Bonetti, G.; Gaburro, Z.; Pavesi, L. Free-Standing Porous Silicon Single and Multiple Optical Cavities. *J. Appl. Phys.* **2003**, *93* (12), 9724.

(46) Solanki, C. S.; Bilyalov, R. R.; Bender, H.; Poortmans, J. New Approach for the Formation and Separation of a Thin Porous Silicon Layer. *Phys. Status Solidi* **2000**, *182* (1), 97–101.

(47) Solanki, C.; Bilyalov, R. Self-Standing Porous Silicon Films by One-Step Anodizing. *J. ...* **2004**, *151* (5), C307.

(48) Goryachev, D. N.; Belyakov, L. V; Sreseli, O. M. Free-Standing Luminescent Layers of Porous Silicon. *Semiconductors* **2010**, *44* (12), 1588–1591.

(49) Iliescu, C.; Jing, J.; Tay, F. E. H.; Miao, J.; Sun, T. Characterization of Masking Layers for Deep Wet Etching of Glass in an Improved HF/HCl Solution. *Surf. Coatings Technol.* **2005**, *198* (1-3 SPEC. ISS.), 314–318.

(50) Caupin, F.; Arvengas, A.; Davitt, K.; Azouzi, M. E. M.; Shmulovich, K. I.; Ramboz, C.; Sessoms, D. a; Stroock, A. D. Exploring Water and Other Liquids at Negative Pressure. *J. Phys. Condens. Matter* **2012**, *24* (28), 284110.

(51) Caupin, F.; Herbert, E. Cavitation in Water: A Review. *Comptes Rendus Phys.* **2006**, *7* (9-10), 1000–1017.

(52) Sumner, A. L.; Menke, E. J.; Dubowski, Y.; Newberg, J. T.; Penner, R. M.; Hemminger, J. C.; Wingen, L. M.; Brauers, T.; Finlayson-Pitts, B. J. The Nature of Water on Surfaces of

Laboratory Systems and Implications for Heterogeneous Chemistry in the Troposphere. *Phys. Chem. Chem. Phys.* **2004**, *6* (3), 604.

(53) Cao, L.; Price, T. P.; Weiss, M.; Gao, D. Super Water- and Oil-Repellent Surfaces on Intrinsically Hydrophilic and Oleophilic Porous Silicon Films. *Langmuir* **2008**, *24* (5), 1640–1643.

Table of Contents Graphic